Magnetic and dielectric properties of Ca^{2+} doped $Bi_{0.9}La_{0.1}FeO_3$ nanoparticles prepared by the sol-gel method

Fang Yang[a,b], Mei Li[a], Hu Yang[a], Jinpei Lin[a,b]*, Kangling Huang[c], Yun He[a,c], Qing Lin[a,b]*

[a]Guangxi Key Laboratory of Nuclear Physics and Nuclear Technology, Guangxi Normal University, Guilin 541004, China.
[b]College of Medical Informatics, Hainan Medical University, Haikou 571199, China.
[c]College of Physics and Technology, Guangxi Normal University, Guilin 541004, China

$Bi_{0.9-x}La_{0.1}Ca_xFeO_3$ ($x=0.05\sim0.25$) nanoparticles were synthesized by an improved sol-gel technique. With an increasing x value, the grain size exhibits an initial drop followed by a subsequent rise. The temperature has a strong effect on the morphology of samples. This implies that 700°C is the optimal temperature for the growth of crystals in the samples. The magnetization increases with an increase in the concentration of Ca^{2+} ions, and the doped crystals exhibit important features of anti-ferromagnetic spin ordering. The remanent magnetization (M_r) exhibits an initial reduction with a subsequent increase versus concentration (x) of Ca^{2+} ions, its minimal value corresponding to $x=0.2$. The substitution of Bi^{3+} ions by Ca^{2+} ions results in the change of the Fe^{3+}-O-Fe^{3+} bond angle, accompanied by a distortion of the oxygen octahedra. With an increase in frequency, multiple Debye peaks appear in all samples, which indicate that the material possesses multiple-frequency energy absorption characteristics. Thus, the frequency-dielectric loss curve is characterized by the superposition of multiple Debye peaks.

Keywords: Perovskite, Sol-gel, Ca^{2+} doping, Structure, Magnetic properties, Dielectric effects

Nowadays, multi-ferroic materials, which simultaneously possess magnetic and ferroelectric properties, have attracted the attention of many researchers due to their potential application in magneto-electric devices[1,2]. Among the various types of multi-ferroic materials, only $BiFeO_3$ (BFO) exhibits ferroelectric and ferromagnetic properties at room temperature. The crystal structure of $BiFeO_3$ was reported to be a G-type anti-ferromagnetic rhombohedrally distorted perovskite structure with R3c space group[3]. In contrast to ordinary anti-ferromagnetic structures, it has a spiral magnetic spin structure along the spatial modulation $(110)_h$ direction with a periodicity of 62 nm. This intrinsic feature allows $BiFeO_3$ to avoid its net magnetization, which leads to net zero magnetization. As a result, $BiFeO_3$ combines weak magnetic properties with large-scale leakage, which inhibit its practical application range[4]. In order to overcome such drawbacks of $BiFeO_3$, researchers have tried various solutions to improve its performance, among which A-site or B-site ion doping seem to be the most effective options. A-site doping mainly involves alkaline earth ions, rare earth ions or their combined usage (co-doping)[5-7], while B-site doping mainly refers to the application of alkaline earth and rare earth ions[8-10]. The most important methods used to prepare $BiFeO_3$ materials are the co-precipitation method[11], sol-gel method[12] and hydrothermal method[13,14]. In this study, $Bi_{0.9-x}La_{0.1}Ca_xFeO_3$ powder was synthesized by the sol-gel method with co-doping by La^{3+} and Ca^{2+} ions, and its structure, morphology, magnetic and dielectric properties were analyzed.

Experimental Procedure

Sample synthesis

This experiment by using polyacrylamide sol-gel synthesis $Bi_{0.9-x}La_{0.1}Ca_xFeO_3$($x=0.05\sim0.25$) nanoparticles. The desired quality of the sample were weighed sample $La(NO_3)_3\cdot6H_2O$, $Fe(NO_3)_3\cdot9H_2O$, $Bi(NO_3)_3\cdot5H_2O$, $Ca(NO_3)_2\cdot4H_2O$, glucose, acrylamide monomer and ethylenediamine tetraacetic acid (EDTA). A variety of nitrate dissolved in nitric acid solution PH=3 to obtain a sol; put sol at 80°C water bath pot stirring, sol becomes wet gel after about 7 h, stirring was stopped. The wet gel was aged for about 12 h, placed blast oven 120°C drying 5 h get xerogel; accelerant (ethanol) was added to the dry gel from spread, get

_____

*Corresponding author
(E-mail: hy@gxnu.edu.cn; elinqing@126.com)

mud yellow fluffy powder. The polishing powder was placed in a crucible, according to the required temperature and time, respectively, calcining at 600°C for three hours to get fluffy yellow mud powder.

Sample characterization

In this experiment, X-ray diffraction (D/max-2500v/pc, Rigaku, Japan) was used to further characterize the structure of the material: the main parameters of the X-ray diffraction process were as follows: pressure pipe, 40 kV; pipe flow, 20 mA; Cu-Kα target radiation; scanning speed is 10°/min; scanning range for 10° to 80° (2θ). Using scanning electron microscopy (NoVa^{TM} Nano 430; FEI,USA) was performed to observe the microstructural properties of LaFeO$_3$ nanomaterial, including particle size, geometrical shape. The magnetic character of the samples was tested with Superconducting Quantum Interference Device (Quantum Design MPMS series XL-7). With this process, we determined the magnetic parameters of samples, including the saturation magnetization (M_s), remnant magnetization (M_r), and coercive force (H_c) values. The measure dielectric parameters of the samples was tested with Microwave network analysis(PNA-N5244A) that was performed from the Keysight, USA.

Results and Discussion

X-ray diffraction

The sample Bi$_{0.9}$La$_{0.1}$FeO$_3$ is a better doping research system[14,15]. The XRD patterns of Bi$_{0.9-x}$La$_{0.1}$Ca$_x$FeO$_3$(x=0.05~0.25) powders are shown in Fig. 1. All the samples are single phase and all the diffraction peaks coincide with the standard perovskite structure (JCPDS card no.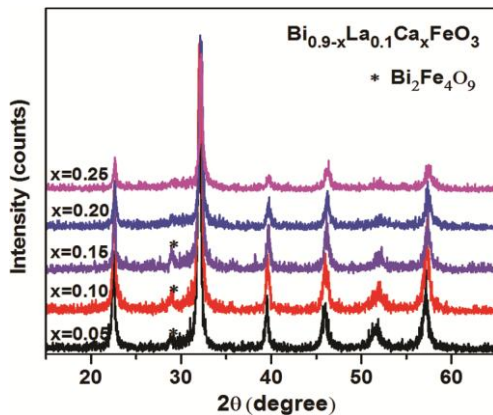 861518) of BiFeO$_3$.A small amount of impurity phase is observed, which can be identified as Bi$_2$Fe$_4$O$_9$[14]. This impurity phase rapidly disappears in the samples with a gradual increase in the Ca content, which implies that the substitution of Bi^{3+} ions by Ca^{2+} ions in Bi$_{0.9-x}$La$_{0.1}$Ca$_x$FeO$_3$ reduces the evaporation of Bi^{3+} ions in the reaction process and effectively suppresses the impurity phase[15].

As seen from Fig. 2, with an increase in Ca^{2+} ion concentration the diffraction peak splitting becomes more pronounced, which indicates an increase of the diffraction angle 2θ with the increase of Ca^{2+} ion concentration, due to the different ionic radii of the dopants. In addition, all diffractograms exhibits, which can be attributed to incomplete formation of the crystalline structure. The diffraction peak half-width β vs x curve exhibits an initial rise followed by the subsequent drop, according to the Scherrer equation[16,17].

$$D = \frac{k\lambda}{\beta \cos\theta} \qquad \dots (1)$$

where k is the Scherrer constant, β is the half-width of the peak, D the grain size, λ the X-ray wavelength and scanning range for 10° to 80° (2θ). It is known that larger values of β correspond to smaller grain sizes and vice versa. This implies that with an increase in x value, the grain size exhibits an initial drop followed by the subsequent rise.

Figure 3 shows the XRD pattern of Bi$_{0.9-x}$La$_{0.1}$Ca$_x$FeO$_3$ (x=0.25) powders calcined at different temperatures. The XRD patterns correspond to the distorted ABO$_3$ P (nm) structure, and Bi$_2$Fe$_4$O$_9$ impurity phases can be seen at calcination temperatures

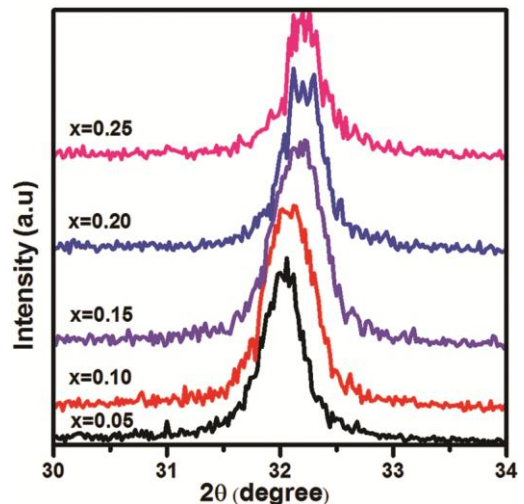Fig. 1 — XRD pattern of Bi$_{0.9-x}$La$_{0.1}$Ca$_x$FeO$_3$ powders calcined at 600°C for 3 h

Fig. 2 — XRD pattern of Bi$_{0.9-x}$La$_{0.1}$Ca$_x$FeO$_3$ powders calcined at 600°C for 3 h

below 600°C. With an increase in temperature, the $Bi_2Fe_4O_9$ impurity phases disappear. In Fig. 2, all samples form a single phase above 600°C, while $Bi_2Fe_4O_9$ impurity phases is observed below 600°C due to the incomplete reaction of the samples at low temperature[18]. In addition, with an increase in calcination temperature, XRD peaks become sharper, but for calcination temperatures higher than 700°C, no further changes in the sharpness of the XRD peaks are observed at higher calcination temperatures. This can be attributed to the fact that at lower temperatures (≤700°C), the sample crystallinity exhibits an increasing trend with temperature, while after reaching 700°C the crystal structure of the sample is already formed and the crystallization process is completed, so that further temperature rise will have no effect on the crystallinity and the XRD pattern. Because of the high temperature, the morphology of samples is irregular. So we choose the sample to calcinate at 600°C for best temperatures[15]. The lattice parameters, average crystallite size, density date of $Bi_{0.65}La_{0.1}Ca_{0.25}FeO_3$ annealed at different temperatures are given in Table 1.

Microstructural characteristics

For getting a deeper insight into the morphology of particles with Bi^{3+} ions substituted by Ca^{2+} ions, the morphology of $Bi_{0.9-x}La_{0.1}Ca_xFeO_3$ (x=0.1, 0.2, 0.25) with calcination temperature of 600°C is depicted in
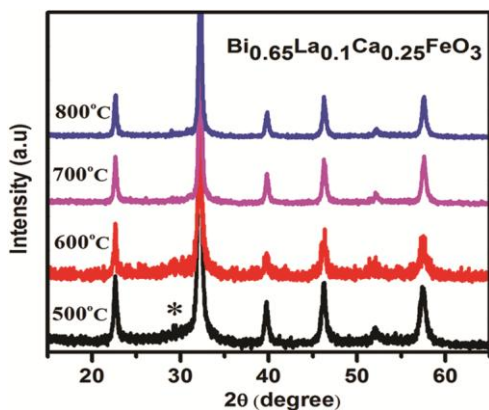

Fig. 3 — XRD pattern of $Bi_{0.9-x}La_{0.1}Ca_xFeO_3$($x$=0.25) powders calcined at different temperatures

Fig. 4, which indicates that an increase in the concentration of Ca^{2+} ions from $x = 0.1$ to $x = 0.25$ results in an initial increase of the particle size, followed by a subsequent reduction. This complies with the XRD analysis results. At x=0.20 idiomorphous crystals with a clear morphology are observed. A further increase of x value results in an initial rise and subsequent drop of the packing density of
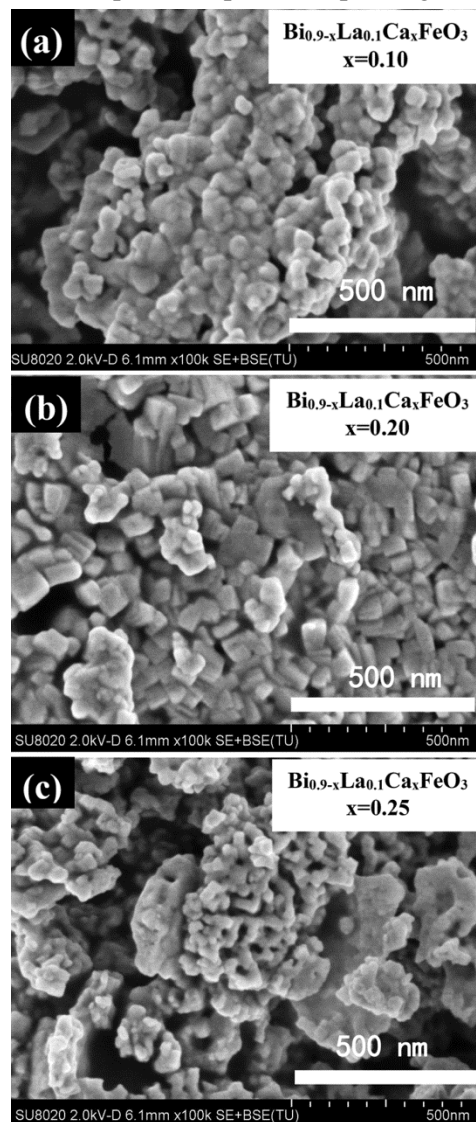

Fig. 4 — SEM of $Bi_{0.9-x}La_{0.1}Ca_xFeO_3$ calcined at 600°C for 3 h

Table 1 — Lattice parameters, average crystallite size, density date of $Bi_{0.65}La_{0.1}Ca_{0.25}FeO_3$ annealed at different temperatures

Temperature(°C)	a (Å)	b (Å)	c (Å)	Vol (Å^3)	Density (g/cm^3)	FWHM	Crystallite (nm)
500	3.9283	3.9283	3.9283	60.62	6.4424	0.433	89.58
600	3.9260	3.9255	3.9244	60.65	6.4322	0.553	89.06
700	3.9231	3.9231	3.9231	60.37	6.4689	0.352	90.36
800	3.9240	3.9240	3.9240	60.81	6.4219	0.367	90.51

the crystallites. Therefore, the optimal morphology of particles is observed at $x=0.20$. Various studies have established that the doping of La is effective in suppressing the formation of oxygen vacancies in $BiFeO_3$. Less oxygen vacancies imply slower oxygen ion motion and consequently lower grain growth rate[15].

Figure 5 presents the topographies of $Bi_{0.65}La_{0.1}$ $Ca_{0.25}FeO_3$ calcined at 500°C, 600°C, 700°C, and 800°C, respectively. The temperature has a strong effect on the morphology of samples. The morphology of particles calcined at 600~700°C is the best, and the grain size is the largest, as compared to other cases. This implies that 600~700°C is the optimal temperature for crystallite growth in the samples under study.

Magnetic properties

The curves of magnetization versus magnetic field (M-H hysteresis loops) of $Bi_{0.9-x}La_{0.1}Ca_xFeO_3$ ($x=0.1$, 0.2, 0.25) with calcination temperature of 600°C are depicted in Fig. 6, from which it can be seen that the area of the M-H hysteresis loop decreases with increasing molar content of Ca^{2+} ions. In particular, at $x=0.25$, the sample behavior is close to paramagnetic. The magnetization increases with an increasing content of Ca^{2+} ions, and the doped crystals exhibit important features of anti-ferromagnetic spin ordering, due to the coupling of ferromagnetic (FM) and anti-ferromagnetic (AFM) properties of the samples[19,20].

The variation of the hysteresis loop parameters of $Bi_{0.9-x}La_{0.1}Ca_xFeO_3$ (x = 0.1, 0.2, 0.25) with the x value is shown in Fig. 7. The coercive force H_c decreases with the content of Ca^{2+} ions due to the magneto-crystalline anisotropy of the sample being

increased with an increasing content of Ca^{2+} ions[21], which eventually leads to a drop in remnant magnetization (M_r)[5,22]. In addition, with an increasing Ca^{2+} ion content, the saturation magnetization M_s also increases. At $x=0.25$, the saturation magnetization still has not yet reached its maximum value. The remanent magnetization M_r versus the Ca^{2+} ion content x exhibits an initial reduction followed by a subsequent rise, while its minimal value of 0.06471 emu/g corresponds to $x=0.2$.

The hysteresis curves of $Bi_{0.65}La_{0.1}Ca_{0.25}FeO_3$ nanoparticles obtained at different calcination temperatures are shown in Fig. 8. At calcination temperatures below 700°C, samples exhibited weak magnetic properties, and their behavior was close to paramagnetic. With an increase in temperature ($T \geq 700°C$), the magnetic properties are enhanced,
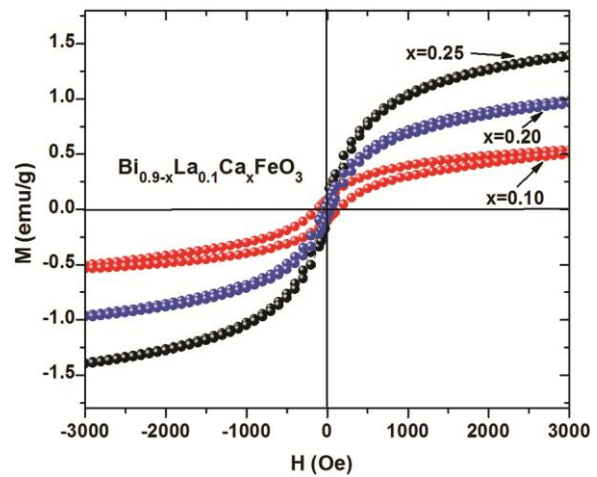

Fig. 6 — Hysteresis loop of $Bi_{0.9-x}La_{0.1}Ca_xFeO_3$ ($x=0.1$, 0.2, 0.25) calcined at 600°C
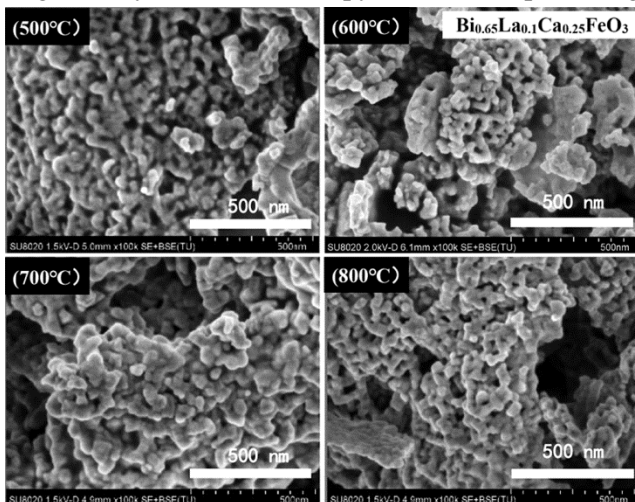

Fig. 5 — SEM images of $Bi_{0.65}La_{0.1}Ca_{0.25}FeO_3$ calcined at different temperatures for 3 h
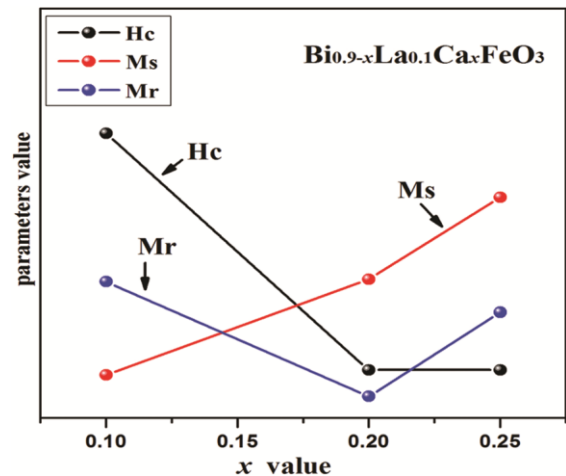

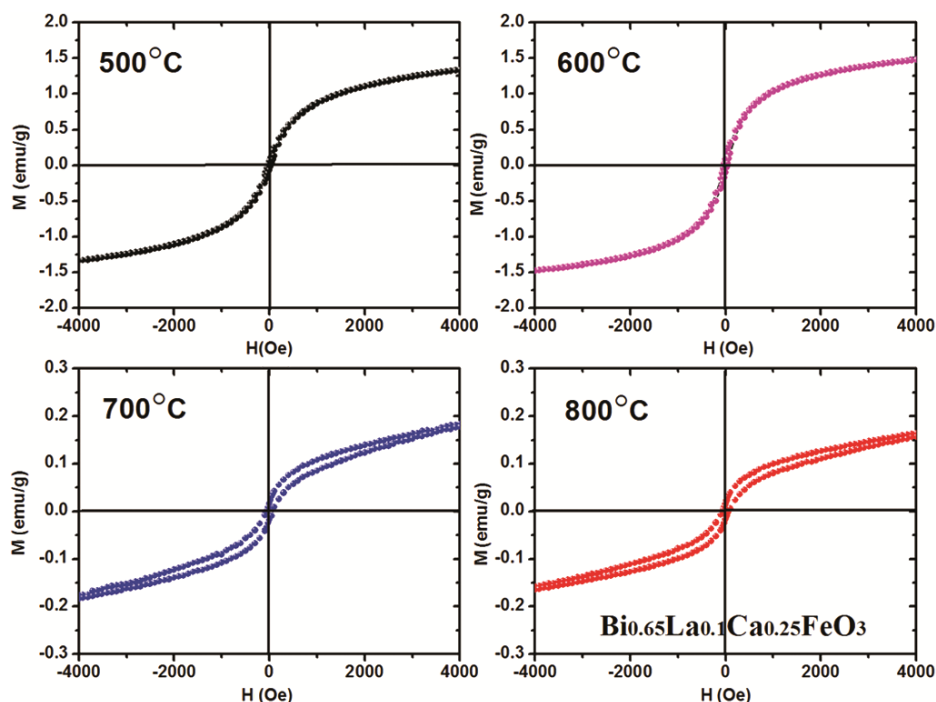Fig. 7 — Hysteresis loop parameters of $Bi_{0.9-x}La_{0.1}Ca_xFeO_3$ versus x value

Fig. 8 — Hysteresis curves of $Bi_{0.65}La_{0.1}Ca_{0.25}FeO_3$ nanoparticles for different calcination temperatures

which is manifested by the hysteresis loop opening, in particular, within the temperature range between 600°C and 700°C. Since the respective curves after calcination at 700°C and 800°C are practically identical, it can be deduced that 600~700°C is the optimal calcination temperature of the samples. This is confirmed by the scanning electron microscopy (SEM) results.

The variation of magnetic parameters of $Bi_{0.65}La_{0.1}Ca_{0.25}FeO_3$ powders produced at different calcination temperatures is depicted in Fig. 9. As long as the calcination temperature is below 600°C, the coercive force H_c of the sample remains unchanged, while a linear H_c-T dependence is observed at higher temperatures. The magnetization (M_s) and remanent magnetization (M_r) of the samples exhibit inverse trends. When the temperature is within the range from 500°C to 700°C, both M_r and M_s values firstly increase a then drop, while above 600°C both remain unchanged. Thus, the calcination temperature has a strong effect on the magnetic parameters of the samples[23,24]. This change in direction has been attributed to the ferromagnetic and anti-ferromagnetic coupling in the sample[22].

Dielectric properties

Figure 10 illustrates the frequency dependence of relative dielectric constant for $Bi_{0.9-x}La_{0.1}Ca_xFeO_3$ (x=0.10, 0.20, 0.25) nanoparticles with calcination
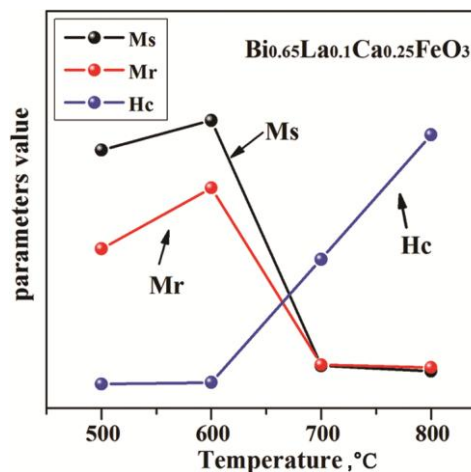

Fig. 9 — Variation of the coercive force H_c, saturation magnetization

temperature of 600°C. It can be seen from this figure that the dielectric constant decreases with frequency f and increases with the doping content-related x value. Since, for a given frequency the dielectric constants at larger x values are higher, Ca^{2+} doping can significantly improve the dielectric properties of $Bi_{0.9-x}La_{0.1}Ca_xFeO_3$[25,26]. The main cause of the change of the dielectric constant with an increase in the Ca^{2+} ion content is as follows: since the ionic radius of Ca^{2+} is smaller than that of Bi^{3+}, the replacement of Bi^{3+} ions with Ca^{2+} ions changes the bond angle of Fe^{3+}-O-Fe^{3+}, leading to a distortion of

the oxygen octahedrons, thus increasing its dielectric constant[27,28].

The frequency dependence of the loss factor (tan δε) for Bi$_{0.9-x}$La$_{0.1}$Ca$_x$FeO$_3$ (x = 0.10, 0.20, 0.25) nanoparticles is shown in Fig. 11. The dielectric loss varies with frequency of Bi$_{0.9-x}$La$_{0.1}$Ca$_x$FeO$_3$, according to the Debye relaxation theory. Multiple Debye peaks appear in all samples with an increase in frequency, which can be explained in terms of the relaxation time dispersion theory as follows: most dielectric materials have no single relaxation time, i.e., the relaxation process is fragmented, and the material has multiple-frequency characteristics of energy absorption. Therefore, the frequency dependence of the dielectric loss is characterized by the superposition of multiple Debye peaks[29].
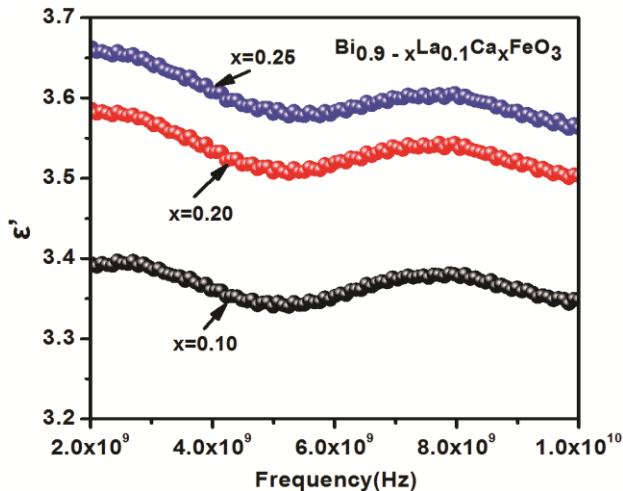

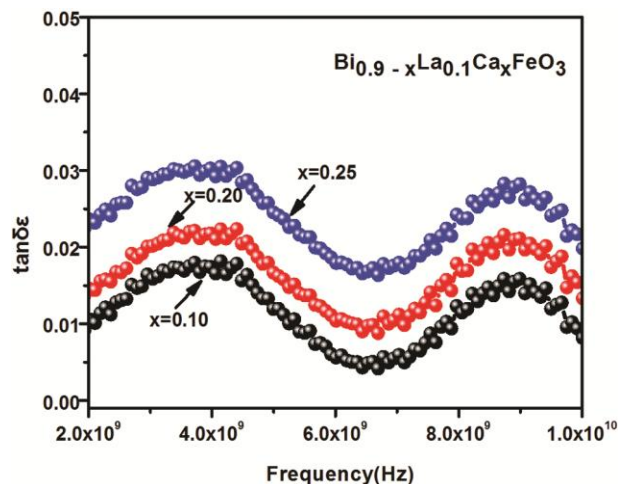Fig. 10 — Frequency dependence of the dielectric constant of Bi$_{0.9-x}$La$_{0.1}$Ca$_x$FeO$_3$

Fig. 11 — Frequency dependence of loss factor (tan δε) for Bi$_{0.9-x}$La$_{0.1}$Ca$_x$FeO$_3$

Conclusions

The Bi$_{0.9-x}$La$_{0.1}$Ca$_x$FeO$_3$ (x=0.05~0.25) nanoparticles were prepared by sol-gel method. The substitution of Bi^{3+} ions by Ca^{2+} ions results in the change of the Fe^{3+}-O-Fe^{3+} bond angle, accompanied by a distortion of the oxygen octahedra. The XRD patterns correspond to the distorted ABO$_3$ P (nm) structure, and Bi$_2$Fe$_4$O$_9$ impurity phases can be seen at calcination temperatures below 600°C. With an increase in temperature, the Bi$_2$Fe$_4$O$_9$ impurity phases disappear. While after reaching 700°C the crystal structure of the sample is already formed and the crystallization process is completed, so that further temperature rise will have no effect on the crystallinity and the XRD pattern. The SEM implies that 700°C is the optimal temperature for crystallite growth in the samples under study. At calcination temperatures below 700°C, samples exhibited weak magnetic properties, and their behavior was close to paramagnetic. With an increase in temperature ($T \geq$ 700°C), the magnetic properties are enhanced, in particular, within the temperature range between 600°C and 700°C. The dielectric constant decreases with frequency f and increases with the doping content-related x value. At a given frequency, Ca^{2+} doping can significantly improve the dielectric properties of Bi$_{0.9-x}$La$_{0.1}$Ca$_x$FeO$_3$.

References

1. Fiebig M, Lottermoser T, Fröhlich D, *et al.*, *Nature*, 419(6909) (2002) 818-820.
2. Fischer P, Polomska M, Sosnowska I, *et al.*, *J Phys C: Solid State Phys*, 13(10) (1980) 1931.
3. Huang Ji-Zhou, Shen Yang, Li Ming & Nan Ce-Wen, *J Appl Phys*, 110 (2011) 094106.
4. Yotburut B, Thongbai P, Yamwong T, *et al.*, *Ceram Int*, 43(7) (2017) 5616-5627.
5. Khomchenko V A, Kopcewicz M, Lopes A M L, *et al.*, *J Phys D: Appl Phys*, 41(10) (2008) 102003.
6. Zhang Y, Zhang H, Yin J, *et al.*, *J Magn Magn Mater*, 322(15) (2010) 2251-2255.
7. Yadav K, Singh M P, Singh H K, *et al.*, *Appl Phys A*, 111(3) (2013) 845-851.
8. Luo L, Shen K, Xu Q, *et al.*, *J Alloys Compnds*, 558 (2013) 73-76.
9. Li Y, Fan Y, Zhang H, *et al.*, *J Superconduct Novel Magn*, 27(5) (2014) 1239-1243.
10. Li J, Liu K, Xu J, *et al.*, *J Mater Sci Res*, 2(3) (2013) 75.

11 Koval V, Skorvanek I, Reece M, Mitoseriu L & Yan H, *J Eur Ceram Soc*, 34 (2014) 641-651.

12 Ren Y, Zhu X, Zhang C, *et al*., *Ceram Int*, 40(1) (2014) 2489-2493.

13 Melo R S, Silva F C, Moura K R M, deMenezes A S & F S M Sinfrônio, *J Magn Magn Mater* , 381 (2015)109-115.

14 Peng-Ting L, Xiang L, Li Z, *et al*., *Chin Phys B*, 23(4) (2014) 047701.

15 Priyadharsini P, Pradeep A, Sathyamoorthy B & Chandrasekaran G, *J Phys Chem Solids*, 75 (2014)797-802.

16 Lin Jinpei, He Yun, Lin Qing, Wang Ruijun & Chen Henian, *J Spectroscopy*, (2014) 540319.

17 Pawan Kumar & Manoranjan Kar, *Mater Chem Phys*, 148 (2014) 968-977.

18 Xie Y J, Guo Y P, Dong W, *et al*., *J Inorg Mater*, 28(4) (2013) 436-440.

19 GeaJ J, Xuea X B, Cheng G F, *et al*., *J Magn Magn Mater*, 324(2) (2012) 200-204.

20 Ahmed M A, Dhahri E, El-Dek S I & Ayoub M S, *Solid State Sci*, 20 (2013) 23-28.

21 Pittala Suresh & Srinath S, *Adv Mater Lett*, 5(3) (2014) 127-130.

22 Lin J, Guo Z, Li M, *et al*. *J Appl Biomater Fundam Mater*, 16(1S) (2018) 93-100.

23 Chauhan S, Kumar M, Chhoker S, *et al*., *RSC Adv*, 6(49) (2016) 43080-43090.

24 Pan D F, Zhou M X, Lu Z X, *et al*., *Nanoscale Res Lett*, 11(1) (2016) 318.

25 Suresh P, Babu P D & Srinath S, *J Appl Phys*, 115(17) (2014) 17D905.

26 Schmeller A, Goñi A R, Pinczuk A, *et al*., *Solid-State Electron*, 37(4-6) (1994) 1281-1284.

27 Catalan G, Sardar K, Church N S, *et al*., *Phys Rev B*, 79, 212415.

28 Yang C, Jiang J S, Wang C M, *et al*., *J Phys Chem Solids*, 73(1) (2012) 115-119.

29 Chang F, Peng H U, Wang D, *et al*., *J Chin Ceram Soc*, 38(6) (2010) 1002-1006.